School of Mathematics & Statistics
Newcastle University

Statistical geometry of the magnetic fields in the multi-phase, turbulent interstellar medium

MAS8091 Report

Cetin Can Evirgen

Supervisors
Professor Anvar Shukurov
Dr Andrew Fletcher

May 2015

Contents

Abstract

This report focuses on the characteristics of the magnetic field and specific entropy, thermal pressure and density in the simulated multi-phase interstellar medium (ISM) of a spiral galaxy. The numerical data available represents the region of the Galaxy similar to the Solar neighbourhood, with a simulation domain of $1 \times 1 \times 2$ kpc in size.

New methods of analysis of the statistical geometry of magnetic field lines are developed to explore the magnetohydrodynamics of the ISM. We conclude that the large-scale characteristics of the galactic magnetic field are highly sensitive to the multi-phase structure of the ISM, whereas the random fluctuations in the galactic magnetic field have similar statistical properties in all the ISM phases.

We have demonstrated quantitatively for the first time, that the large-scale interstellar magnetic field is hosted by the warm phase of the ISM.

Acknowledgments

I would like to thank my supervisors Professor Anvar Shukurov and Dr Andrew Fletcher for their support and encouragement throughout my MMath research project and throughout my undergraduate degree. I look forward to working with them, Dr Paul Bushby and the ISM group at Newcastle in the future.

I would like to thank Dr Frederick Gent for taking on the mammoth task of building the numerical model of the ISM, which has provided a wealth of simulated astrophysical data. I have thoroughly enjoyed our collaborative work and look forward to working together in the future.

With the support given by Dr Michael Beaty and Dr Chris Graham, on the computational requirements of the project, my poor laptop has survived the year and my code runtime has improved by an order of magnitude. I am exponentially grateful.

I would like to thank Dr Luiz Felippe Santiago Rodrigues and Dr Frederick Gent for helping me understand and use the vast datasets generated by the numerical simulations.

I would like to thank my lecturers for inspiring me and instilling the fear of words such as "trivial" in me over the last four years; the administrative staff for making sure we stay on the straight and narrow; my friends and coursemates for sharing both the good times and for suffering through the "trivial" algebra together.

I love and thank my family for their unconditional love and support through thick and thin.

I dedicate this report to the loving memory of my grandfather, Cetin Evirgen.

Chapter 1

Introduction

1.1 Galaxies and the interstellar medium

A spiral galaxy has a quasi-spherical bulge in the centre and a thin disc of stars and gas. Many galaxies have a bar, a non-axisymmetric structure in the inner part. Figure 1.1(b) shows a cross-sectional diagram of the Milky Way, a barred spiral galaxy (Eckart and Englmaier, 2002). There is a tenuous gas between stars, referred to as the interstellar medium (ISM). Star formation occurs in the colder regions of the ISM. The ongoing star formation produces supernovae. Their explosions drive random motions in the ISM and generate its prominent multi-phase structure, with cold, warm and hot phases being most conspicuous.

1.1.1 The multi-phase interstellar medium

Temperatures of $T = \mathcal{O}(10^2\mathrm{K})$ are typical of the cold, dense star-forming regions of the ISM, whereas temperatures in the range $T = \mathcal{O}(10^2\text{–}10^5\,\mathrm{K})$ and $T = \mathcal{O}(10^5\text{–}10^6\,\mathrm{K})$ are typical of the warm and hot phases, respectively. Similarly wide ranges are spanned by density, random gas speed and thermal pressure. The ISM cannot be clearly separated into thermodynamic phases in physical terms. However, it is equally clear that we cannot expect uniformity of characteristics across the vast length scales, time scales and magnitudes of physical variables observed throughout the ISM.

Many numerical models (Korpi et al., 1999; de Avillez and Breitschwerdt, 2005; Gent, 2012; Hill et al., 2012) of the ISM have been explored, particularly in the last two decades, with the increasing availability of high-power computers. The numerical simulation of the multi-phase ISM carried out by Gent (2012) and Gent et al. (2013a,b) (hereafter referred to as Paper I and Paper II), has provided rich data that will be used in this report. The model incorporates a broad range of physical phenomena, with good physical and time resolution, over a sufficiently

(a)

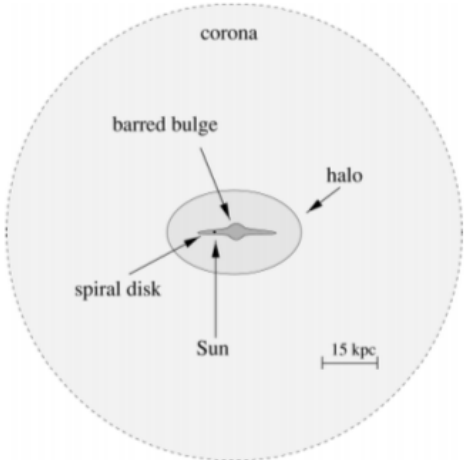

(b)

Figure 1.1: **(a)** The Milky Way Galaxy viewed from above. **(b)** A cross-sectional diagram of the Milky Way (Eckart and Englmaier, 2002).

large simulation domain. Twelve data snapshots are available for the model, over an identical domain. Each snapshot is sufficiently separated in time, to ensure time-independence. Further discussion of the model is given in Section 1.2. One of the unique features of this model is the self-consistent treatment of magnetic fields in the multi-structure of the ISM.

1.2 Numerical models of the ISM

1.2.1 The simulation domain

The simulation domain of Paper I and Paper II is a box 1×1 kpc^2 horizontally (x, y) extending 2 kpc vertically (z) centred about the Galactic midplane, such that $|z| \leq 1$ kpc. The box is situated in the disc within a spiral galaxy. Here Galactic (capitalised) refers to the Milky Way, whereas galactic refers to a general galaxy. This distinction is made since the model parameters are taken from observational values from the Galaxy, where observational data is currently most abundant (Gent, 2012; Eckart and Englmaier, 2002).

1.2.2 Physical ingredients of the model

This section is intended to motivate the analysis developed in this report, without providing an exhaustive discussion of the numerical model. The PENCIL

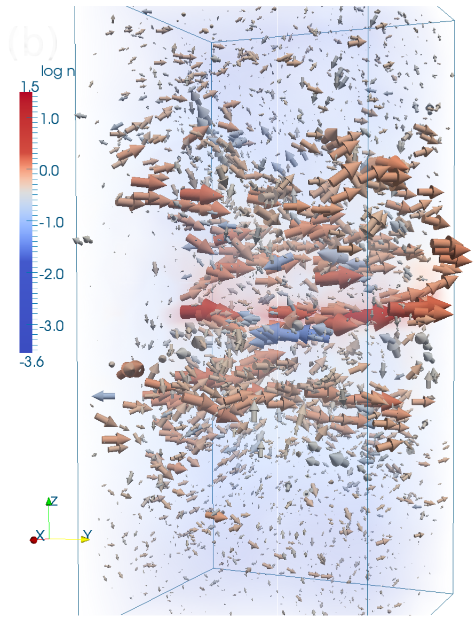

Figure 1.2: 3D rendering of the box featuring quiver plots of the mean magnetic field. The image is taken from the (Gent, 2012).

CODE (Brandenburg et al., 2001) is used to solve the set of fully non-linear, compressible MHD equations, which include the mass conservation equation, the Navier-Stokes equation, the heat equation and the induction equation (Gent, 2012). These equations are solved in a rotating frame of reference with differential rotation similar to the Solar vicinity of the Galaxy. Whilst differential rotation does not affect random gas velocities strongly in the ISM, it has been observed that the magnetic field is strongly aligned with the spiral arms of the galaxy (Tabatabaei et al., 2008; Fletcher et al., 2011), which creates a predominantly azimuthal magnetic field. Thus, inclusion of differential rotation is necessary to create realistic physical conditions for the evolution of the galactic magnetic field.

Supernova explosions (SNe) occur within approximately ± 50 pc of the mid-plane in regions of cold, dense gas. The SNe release large amounts of energy, forming SN remnants that expand out of the box in the vertical (z) direction at transonic speeds. Since the ISM is highly compressible, these explosions often form shock fronts as they travel through the ISM. Expansion of the SN remnants and the shock fronts distort the magnetic field.

Random (turbulent) flows driven by the SNe combine with the differential rotation to further distort the magnetic field and, importantly, generate its non-random, large-scale component.

1.2.3 Limitations of model

Vertical extent of the simulation domain

The numerical resolution required to capture the dynamics of the ISM is obtained at the cost of limiting the vertical extent of the box. Consequently, the box does not extend sufficiently far above the midplane to analyse the dynamics of the hot gas travelling towards the halo (Gent, 2012). This generally requires a vertical domain extending ± 10 kpc above the galactic midplane (de Avillez and Breitschwerdt, 2004). It has been reported by de Avillez and Breitschwerdt (2004), that the ISM consists entirely of hot gas at $|z| > 2.5$ kpc. Nevertheless, the simulation box of Gent (2012) extends to a sufficient length to analyse the gas dynamics at the galactic midplane (Gent, 2012).

Cosmic rays

The current numerical model does not include cosmic rays. It is believed that cosmic rays are generated and accelerated in and around SN remnants (Gent, 2012). Hence, it is interesting to investigate the the effect of cosmic rays on magnetic field distortion.

Current work in the Newcastle ISM group has shown that cosmic rays increase magnetic buoyancy. In addition, cosmic ray propagation is controlled by magnetic fields (Kulsrud, 1978; Gent, 2012). The initial omission of cosmic rays allows a separate analysis of the effect of the multi-phase structure on the galactic magnetic field. The methods presented in this report will be applicable to the numerical model featuring cosmic rays. Further discussion of future work on the effects of cosmic rays is given in Section 4.

1.2.4 Aims and objectives

As previously mentioned in Section 1.2.2, it is necessary to analyse the interaction between the galactic magnetic field and turbulent flows in the ISM, in order to understand the gas magnetohydrodynamics. Current tools of analysis, such as Fourier spectra and various structure and correlation functions only provide a general analysis of the dynamics of the ISM; they are not able to capture the full complexity of the gas flows and magnetic fields in the ISM.

We are interested in whether the magnetic field is sensitive to the multi-phase structure. How does the magnetic field and other physical variables behave in the highly compressible, turbulent flows observed in the galaxy? In this report, we present statistical techniques for analysing the geometry of integral lines of the magnetic field. In Chapter 2, the main methods are presented and discussed.

Following this, we present the main results of the report in Chapter 3. Final remarks on the topic are given in Chapter 4 to motivate future work.

Chapter 2

Methods

The general methods of analysis used in the report are introduced in this section together with the limitations of the methods and planned technical improvements. Conceptual improvements will be discussed in Section 4.

2.1 The mean magnetic field and averaging

In this section, we consider the magnetic field to have a mean (large-scale) component and a random (fluctuating or small-scale) part. The mean field can be obtained by time, spatial or ensemble averaging. Time averaging is not used due to the multi-phase structure of the ISM; the locations of the phases change over time. Time averaging at some $\boldsymbol{x} \in \mathcal{D}$, where $\mathcal{D}$ refers to the simulation box, over different snapshots can lead to loss of information. For example, $\boldsymbol{x}$ could be located in a cluster of cold gas at some time but in the warm phase at another time. Hence, time averaging is not a suitable method in this environment (Tennekes and Lumley, 1972, p. 28).

Instead, spatial averaging is commonly used, particularly horizontal averaging, where an average is taken over the xy-plane at each $z \in [z_{\min}, z_{\max}]$. This approach assumes homogeneity of the mean field in the plane. However, horizontal averages combine data from different phases. It is more appropriate to average along magnetic field lines. Physically meaningful ensemble averages can be derived from samples along the field lines.

2.1.1 Gaussian smoothing and its implementation

The total magnetic field can be decomposed into the mean, $\langle \boldsymbol{B} \rangle_l$, and random, $\langle \boldsymbol{b} \rangle_l$, parts using Gaussian smoothing,

$$\boldsymbol{B} = \langle \boldsymbol{B} \rangle_l + \boldsymbol{b}_l, \tag{2.1}$$

where

$$\langle \boldsymbol{B}(\boldsymbol{x}) \rangle_l = \int_{\mathcal{D}} \boldsymbol{B}(\boldsymbol{x'}) G_l(\boldsymbol{x} - \boldsymbol{x'})\,\mathrm{d}^3\boldsymbol{x'} \tag{2.2}$$

is the convolution of the magnetic field with a Gaussian kernel $G_l(\boldsymbol{x})$ of scale l, given by

$$G_l(\boldsymbol{x}) = (2\pi l^2)^{-3/2} \exp[-\boldsymbol{x}/(2l^2)].$$

The smoothing process can be viewed as a Gaussian kernel being moved around the domain and picking up a weighted average of the data. Let us consider a simple example of Gaussian smoothing in one dimension (which can be extended to higher dimensions without difficulty), applied to the Dirac delta function at some point $x = a$,

$$\begin{aligned}
\langle \delta(x-a) \rangle_l &= \int_{-\infty}^{\infty} \delta\left(x' - a\right) G_l\left(x - x'\right)\,\mathrm{d}x', \\
&= \frac{1}{\sqrt{2\pi l^2}} \int_{-\infty}^{\infty} \delta(x'-a) \exp\left[(x-x')/2l^2\right]\,\mathrm{d}x', \\
&= \frac{1}{\sqrt{2\pi l^2}} \exp\left[(x-a)^2/2l^2\right].
\end{aligned}$$

As the Gaussian kernel is convolved with a point mass, it essentially focuses itself at the mass location whilst preserving the kernel scale l, as shown in Fig. 2.1. Gent (2012) and Paper II suggest the the optimal kernel size to be $l = 50$ pc, which has been used in this report. An in-depth discussion of this choice is given in Section 8 of the Gent (2012). Two approaches are explored; one based on the magnetic field energy densities of the mean and random field and another based on their Fourier power spectra. Preliminary work carried out for this research project, examining integral lines of the mean and random magnetic field, show that kernel size in the range $l > 50$ pc has little effect on the features of the mean or random field. Below $l = 50$ pc, the random field begins to develop longer, filamentary features of greater length. These features can be parts of the large-scale structure that are being missed by choosing a kernel of insufficient size.

Gaussian smoothing is implemented using functions, **gaussian_filter1d** in 1D and **gaussian_filter** in 3D, of the SciPy Image Processing package (Verveer, 2003) in Python. As part of preliminary work, these functions were tested with simple cases up to three dimensions, with a simple one-dimensional example displayed in Fig. 2.1. Initially, a three-dimensional Gaussian smoothing (**gaussian_filter**) was used, with good overall accuracy. However, this algorithm requires the boundaries to be treated in the same way in all dimensions. This required either to "wrap" the boundaries around and treat the data as being periodic or to reflect the boundary values into a "ghost zone" to compute values close to and at the boundary. In the numerical model developed by Gent (2012), periodic boundary conditions are

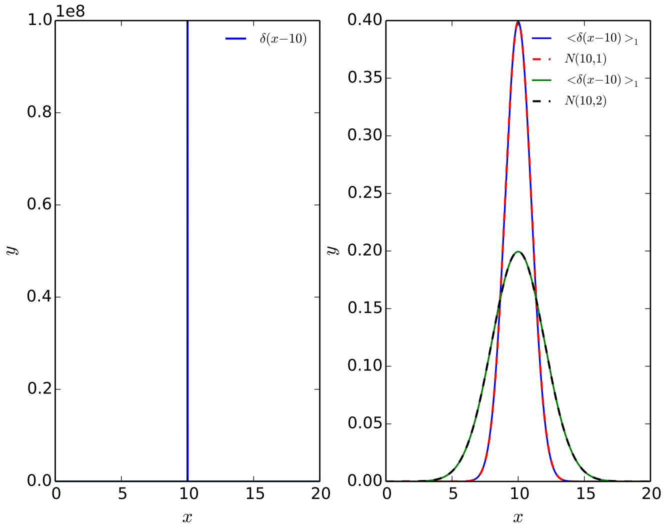

Figure 2.1: An approximation to $\delta(x-10)$ (left panel) smoothed (right panel) with Gaussian kernels of scale 1 (blue solid) and 2 (green solid), with analytically calculated curves overlaid, red dashed and black dashed, respectively.

applied in the xy-plane but not in the z-direction, as required to allow for gas outflows.

An alternative numerical smoothing routine has been developed to account for these boundary conditions, using a succession of one-dimensional Gaussian kernels along each axis, as described in the following section.

Decomposition of three-dimensional Gaussian smoothing

To perform Gaussian smoothing in a non-periodic domain, we apply three consecutive Gaussian filters,

$$
\begin{aligned}
G_{l,3}(\boldsymbol{x}-\boldsymbol{x'}) &= \frac{1}{(2\pi l^2)^{3/2}} \exp\left[\frac{1}{2l^2}(\boldsymbol{x}-\boldsymbol{x'})\cdot(\boldsymbol{x}-\boldsymbol{x'})\right], \\
&= \frac{1}{(2\pi l^2)^{3/2}} \exp\left[\frac{1}{2l^2}\sum_{i=1}^{3}(x_i-x_i')^2\right], \\
&= \prod_{i=0}^{3} \frac{1}{(2\pi l^2)^{1/2}} \exp\left[\frac{(x_i-x_i')^2}{2l^2}\right], \\
&= \prod_{i=0}^{3} G_{l,1}(x_i-x_i').
\end{aligned}
$$

Then, the Gaussian smoothing of a component of the magnetic field is now expressed as,

$$\langle B_i(x,y,z)\rangle_l = \int G_{l,1}(x-x')dx' \int G_{l,1}(y-y')dy' \int B_i(x',y',z')G_{l,1}(z-z')\,\mathrm{d}z',$$

over the box, $\mathcal{D}$, by appealing to Fubini's Theorem, which implies that an n-dimensional integral can be calculated as a succession of n one-dimensional integrals. In this report, the magnetic field is smoothed in the z-direction first, with boundaries treated with reflection. Gaussian filters in the x and y axes are then applied with periodic boundary conditions. The smoothing routine acts on each component of the magnetic field separately. Having obtained the mean magnetic field, we obtain the random magnetic field as

$$\boldsymbol{b}_l = \boldsymbol{B} - \langle \boldsymbol{B}\rangle_l \,.$$

2.2 Integral lines of the magnetic field

Integral lines of the magnetic field (field lines) in Cartesian coordinates are are defined via Parker (2013):

$$\frac{dx}{B_x} = \frac{dy}{B_y} = \frac{dz}{B_z}. \tag{2.3}$$

Magnetic field lines are considered to be the path that a point charge follows along the direction of the magnetic field (Parker, 2013). It is similar to streamlines in a fluid flow, where a small particle traces out a path along a particular line of fluid velocity.

It is tempting the treat Eq. (2.3) as two differential equations, reducing the problem from an equation of three terms to two separate equations, for example

$$\begin{cases} \dfrac{dy}{dx} = \dfrac{B_y}{B_x}, \\ \dfrac{dz}{dx} = \dfrac{B_z}{B_x}. \end{cases}$$

However, this representation leads to loss of information since it is sensitive only to the ratios of the field components. Field lines obtained via these equations exhibit artificial discontunities, arising from the parameterisation of Eq. (2.3) in terms of x.

Instead, we parameterise the field lines in terms of the arc length, s, which avoid forcing the movement of the field lines along any of its components. The intregral line equations become (Parker, 2013)

$$\frac{dx_i}{ds} = \frac{B_i}{|\boldsymbol{B}(\boldsymbol{x})|}, \tag{2.4}$$

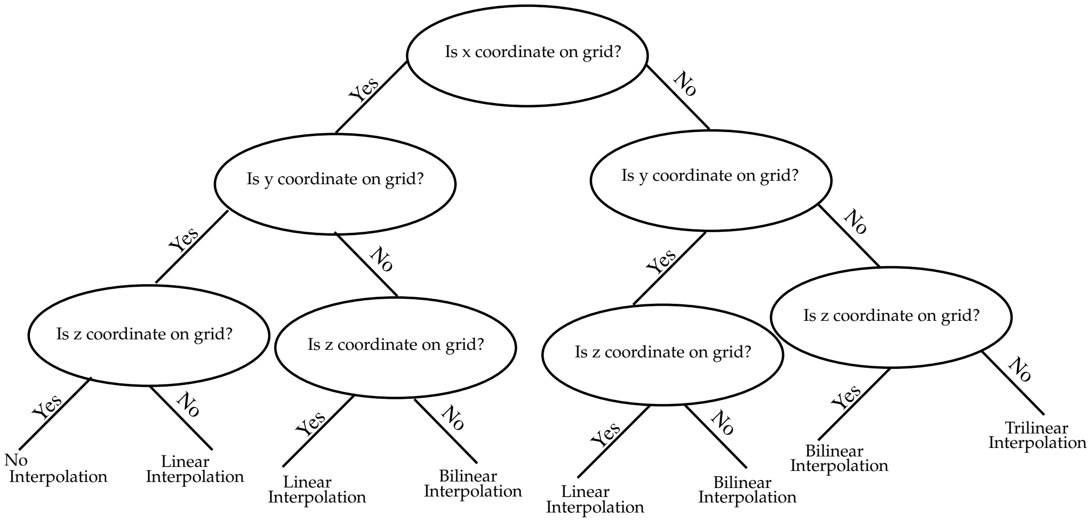

Figure 2.2: Interpolation flowchart

where $|\boldsymbol{B}(\boldsymbol{x})|$ is the magnetic field strength at the current point of the field line.

2.2.1 Field line integration

The field line equations (2.4) are modified for the numerical routine, cast in terms of finite increments Δx_i and Δs

$$\Delta x_i = \frac{B_i}{B_V} \Delta s, \tag{2.5}$$

where we fix $\Delta s = 4 \times 10^{-3}$ kpc, the numerical resolution of the model. This equation is solved using a Runge-Kutta fourth-order numerical integration method for each component of the field. The method is adapted from lecture material of the module MAS8122 (Sarson, 2014).

Interpolation

Linear interpolation is used to derive values of $\boldsymbol{B}$, which do not lie on the data grid (Bourke, 1997). The algorithm chooses the type of interpolation to be applied, based on the flowchart in Fig. 2.2. This flowchart has been written to limit the interpolation applied. For example, if the x and y coordinates lie on the grid, interpolation is used only along the z-axis. Whilst different interpolation methods might be considered, linear interpolation is sufficiently accurate over the interpolation cell given in Fig. 2.3(a). As shown in Fig. 2.3(b), P will be at most $6\sqrt{3}$ pc away from any vertex of the interpolation cell, which is less than twice the numerical resolution of the model.

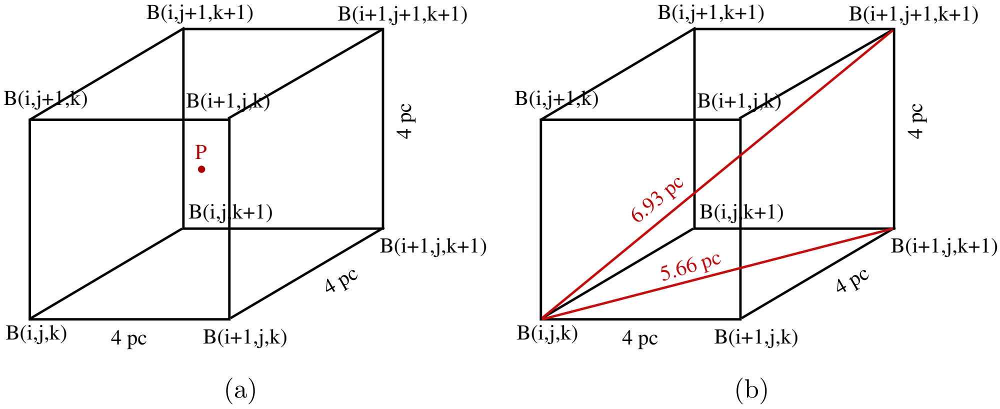

Figure 2.3: **(a)** The current point, P, contained within an interpolation cell **(b)** Distances within a typical interpolation cell.

Selection of seed points for magnetic field lines

The mean magnetic field is strongly aligned in the azimuthal (y) direction because of the velocity shear across the computational domain that models the differential rotation (Gent, 2012). Hence, we launch magnetic field lines from various positions in xz-plane at $y = -0.5$ kpc for the mean field. For the random field, the correlation scale (discussed in Section 3) is smaller in general. Thus, more seed planes in various xz-planes are used to ensure the whole box is sampled. A sketch of the seed point set up is given in Fig. 2.4, which also shows the separation between seed points. This separation was initially chosen to be 320 pc, to ensure statistical independence of field lines, which is six times larger than the kernel scale for Gaussian smoothing and larger than the correlation scale reported (Gent (2012), Paper II). Over-sampling of the box is prevented for the mean magnetic field line by only seeding along a single xz-plane at $y = -0.5$ kpc (at a face of the box). For both fields, the integration algorithm is instructed to stop if a field line travels within 1 pc of any point along itself. Here, the 1 pc allowance is a factor of 4 smaller than the numerical resolution. Having tried 320 pc, we found that 160 pc separation between seed points does not have produce any artifical features of the integral line obtained. Hence, a seed separation of 160 pc is used in this report. Nonetheless, future work will focus on a more detailed analysis of variations in the seed point separation to maximise the amount of data used in analysis, whilst ensuring that over-sampling does not occur.

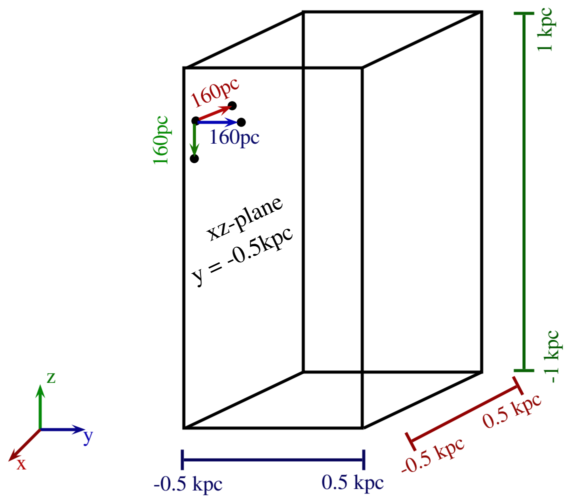

Figure 2.4: The black dots represent example seed points, with seed point separation of 160 pc in each direction in the xz-plane for the mean magnetic field and along each coordinate direction for the random field.

2.3 Sampling along field lines

The magnetic field lines can also be used for analysis of geometric properties of the magnetic field. Whilst the primary focus of this report is on the statistical methods for analysing general characteristics of the ISM, preliminary methods and results developed for the analysis of the statistical geometry of the magnetic field are also presented. These results are intended give an indication of the questions that we wish to answer and the challenges they present.

Furthermore, we sample specific entropy of the ISM gas along the magnetic field lines, which enables an analysis of the charactertistics of the magnetic field and other physical variables in the multi-phase structure, with specific entropy.

2.3.1 Ensemble averaging along field lines

Once we have obtained the sampled variables separately along mean and random field lines, the respective sets of samples are combined to form an ensemble average. This allows statistical properties of the physical fields to be derived. In addition, it enables the isolation of data pertaining to individual ISM phases before time averaging over the different snapshots.

The averaging method is based on ideas from stereology (Baddeley and Jensen, 2004), where the equivalence of averaging over volume, area and along lines is established. The field lines are calculated from the same governing equations, each region of the box is sampled across multiple snapshots and the seed points are identical for each snapshot. We argue that this represents a robust spatio-temporal ensemble average of the magnetic field and other physical variables such as specific entropy. We believe that it is more sensible to average along field lines, than using either spatial or temporal averages alone. We note that simple spatial averages such as horizontal averaging are not sensitive to the multi-phase structure and can be especially misleading in the case of the magnetic field lines as they are free to move from one phase to another.

Moreover, the samples can be combined across snapshots without superimposing data from different phases. Having combined the data from the ensemble averages, probability density functions (PDF) are constructed. These are used to analyse the physical variables statistically.

2.3.2 Probability density functions (PDFs)

Histograms

The samples of physical variables along magnetic field lines are stored as one-dimensional data sets for each data snapshot. For a simple dataset, a histogram is the most obvious choice for an effective graphical representation. If we have N measurements of the random variable being sampled, then the histogram converges to the statistical distribution (the PDF) in the limit $N \to \infty$ if the bin width decreases with N (CFD, 2007). The number of realisations, N, is determined by the sampling of the data. We sample values across 12 samples and typically have $N \sim \mathcal{O}(10^2 - 10^5)$. The lower bound $N \sim \mathcal{O}(10^2)$ is observed for the cold phase, which has a fractional volume one and two orders of magnitude smaller than the warm and cold phases, respectively. As expected, we observe $N \sim \mathcal{O}(10^3 - 10^4)$ for the warm phase and $N \sim \mathcal{O}(10^5)$ for the hot phase. Smaller scale fluctuations in the fractional volume correspond to commensurate fluctuations in N. There is not an obvious general method for adjusting bin widths to take into account differences in N.

An inappropriate choice of bin locations can cause discontinuities in the histogram, which are not representative of the underlying statistical distribution (Gutierrez-Osuna, 2013). Consequently, we consider a different approach to construct the PDFs.

Gaussian kernel density estimation

Gaussian kernel density estimation (KDE) is used to estimate the statistical distribution of data using a linear combination of Gaussian kernels, centred at the data points, say x_i. This circumvents complications associated with choosing bins for histograms (Gutierrez-Osuna, 2013). KDE is a non-parametric method, which enables the calculation of PDFs without making assumptions about samples of complex data sets. An important aspect of KDE is the ‘bandwidth’ of Gaussian kernels used. This determines the width of the kernels centred at each data point and affects the shape of the PDF estimate. A large bandwidth can cause the data to be smoothed excessively, whereas a small bandwidth can cause the PDF to be too spiky (Gutierrez-Osuna, 2013). The Gaussian KDE is used to calculate PDFs

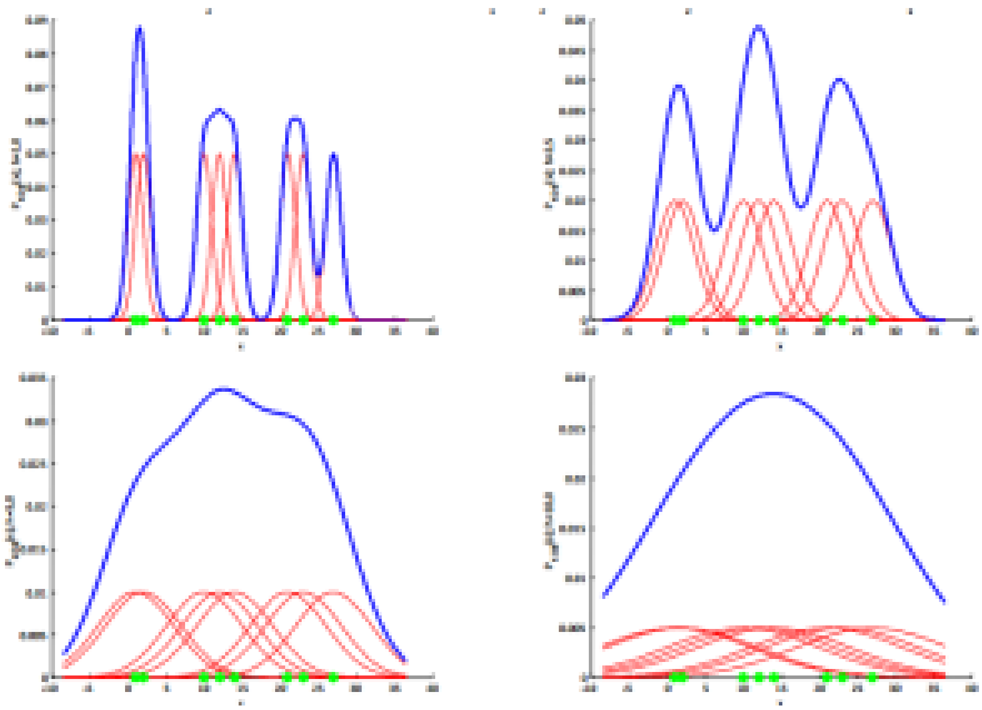

Figure 2.5: An example of Gaussian kernel density estimation. The green dots along the horizontal axes represent the data points. The red curves represent the kernels fitted at the data points and the blue curves are the resultant kernel density estimates. The top panel shows the spikes created by using a small bandwidth. The bottom panel shows the oversmoothing caused by using a large bandwidth. Image from Gutierrez-Osuna (2013).

for this report. It is implemented using the SciPy function *gaussian_kde* (Kern, 2005). The bandwidths are calculated using Scott’s Rule, given by

$$N^{-1/(d+4)},$$

where N is the number of data points and $d = 1$ is the number of dimensions in the data.

2.4 An alternative approach to analysis of correlation lengths

For any random field, structure and correlation functions are the main analytical tools developed for statistical analysis of turbulent flows (Tennekes and Lumley, 1972). The following structure function of the the magnetic field, $\boldsymbol{B}$, is defined as

$$\mathcal{D}(l) = \left\langle [\boldsymbol{B}(\boldsymbol{x}+\boldsymbol{l}) - \boldsymbol{B}(\boldsymbol{x})]^2 \right\rangle, \tag{2.6}$$

where $l \equiv |\boldsymbol{l}|$ and angular brackets denote ensemble averaging. The structure function can be used to construct the autocorrelation function

$$\mathcal{C}(l) = 1 - \frac{\mathcal{D}(l)}{2\sigma_B^2}, \tag{2.7}$$

where σ_B^2 refers to the or variance of the magnetic field energy density. The autocorrelation function can be used to find characteristic scales of the random field, most importantly the correlation length,

$$L = \int_0^\infty \mathcal{C}(l)\mathrm{d}l.$$

However, such a calculation meets significant difficulties when the data are known in a finite region.

Instead of calculating correlation lengths via structure functions, we propose a method which takes into account the sensitivity to the multi-phase structure. Fig. 2.6(a) shows an example of a field line calculated over $N+1$ steps labelled with $i = \{0, 1, 2, \ldots, N\}$. This field line is characterised by two lengths; the maximum displacement of the field line from the seed point, $\mathcal{R}$, and the total length of the field line, $\mathcal{L}$:

$$\mathcal{R} = |x_{\max} - x_0|, \tag{2.8}$$

where $x_{\max}$ is the furthest point away from the seed point, and

$$\mathcal{L} = \sum_{i=0}^{N-1} |x_{i+1} - x_i| = s_{\max} - s_{\min}. \tag{2.9}$$

Let us examine the two expressions. Firstly,

$$\boldsymbol{x_j} = \boldsymbol{x_0} + \sum_{i=0}^{j-1} \frac{\boldsymbol{B}(\boldsymbol{x_i})}{|\boldsymbol{B}(\boldsymbol{x}_i)|} \Delta s,$$

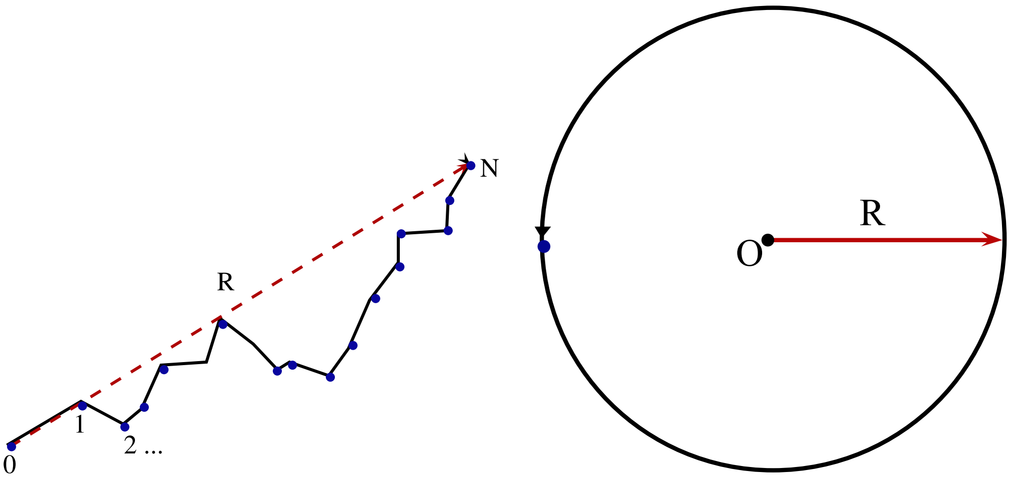

(a) (b)

Figure 2.6: **(a)** An example of a field line (black solid) with each vertex (blue dot) representing $\boldsymbol{x_i}$, where $i = \{0, 1, 2, \ldots, N\}$. $\mathcal{R}$ is the maximum displacement from the seed point of the field line. In this example, the furthest point is at the end of the field line. However, the maximum displacement could occur at any point along the field line. **(b)** An example of a planar, circular field line, centred at the origin O with radius R.

where $j = 1, 2, \ldots, N$ and it is clear that there is a choice of j such that $|\boldsymbol{x_j} - \boldsymbol{x_0}|$ is maximised. Let us assume this is some $j = k \in 1, 2, \ldots, N$, then

$$\mathcal{R} \equiv |\boldsymbol{x_k} - \boldsymbol{x_0}| = \left| \sum_{i=0}^{k-1} \frac{\boldsymbol{B}(\boldsymbol{x_i})}{|\boldsymbol{B}(\boldsymbol{x}_i)|} \Delta s \right| = \Delta s \left| \sum_{i=0}^{k-1} \frac{\boldsymbol{B}(\boldsymbol{x_i})}{|\boldsymbol{B}(\boldsymbol{x}_i)|} \right|.$$

Similarly, $\mathcal{L}$ can be expressed as

$$\mathcal{L} = \Delta s \sum_{i=0}^{N-1} \left| \frac{\boldsymbol{B}(\boldsymbol{x_i})}{|\boldsymbol{B}(\boldsymbol{x}_i)|} \right|.$$

We note that $\mathcal{L} \geq \mathcal{R} \geq 0$ must hold for any magnetic field line since

$$\sum_{i=0}^{N-1} |\boldsymbol{B}(\boldsymbol{x_i})| \geq \left| \sum_{i=0}^{N-1} \boldsymbol{B}(\boldsymbol{x_i}) \right|.$$

Then, $\mathcal{L}$ is simplified to

$$\begin{aligned} \mathcal{L} &= \Delta s \sum_{i=0}^{N-1} \left| \frac{\boldsymbol{B}(\boldsymbol{x_i})}{|\boldsymbol{B}(\boldsymbol{x}_i)|} \right|, \\ &= \Delta s \sum_{i=0}^{N-1} \frac{|\boldsymbol{B}(\boldsymbol{x_i})|}{|\boldsymbol{B}(\boldsymbol{x}_i)|}, \\ &= \sum_{i=0}^{N-1} \Delta s \equiv s, \end{aligned}$$

the arc length of the field line, as expected. The dimensionless quantity $0 \leq \mathcal{R}/\mathcal{L} \leq 1$ is a measure of the curvature of the field line. For example, Fig. 2.6(b) shows a planar, circular field line; it has $\mathcal{R} = 2R$ and $\mathcal{L} = 2\pi R$. Thus, its measure of curvature is $\mathcal{R}/\mathcal{L} = 1/\pi$. It is clear that these geometrical arguments can be extended to three physical dimensions and set in different coordinate systems to establish analytical values for different types of field lines.

In this report, we treat $\mathcal{R}$ as the correlation scale of the magnetic field line. Future work will consider the significance of $\mathcal{L}$. The PDF of $\mathcal{R}$, $\mathcal{P}(\mathcal{R})$, is constructed using the magnetic field lines from the twelve snapshots available. The correlation length is then calculated as

$$\mathcal{C} = \int_0^{r_{\max}} r\mathcal{P}(r)\,\mathrm{d}r, \tag{2.10}$$

where $r_{\max}$ is the maximum $\mathcal{R}$ measured throughout all field lines from all data snapshots.

Chapter 3

Results

The main results of this research project are presented in this chapter. Whilst the focus will be on the magnetic field, we also discuss other properties of the ISM gas, such as density, temperature and thermal pressure, in order to give a fuller explanation of the characteristics of the magnetic field.

3.1 Visualising the mean magnetic field lines

The mean magnetic field lines are contructed as described in Section 2.2 and a 3D visualisation is given in Fig. 3.1. The white lines in the box represent the mean magnetic field lines.

Figure 3.1(b) makes it especially the ISM gas is stratified, as expected from the ISM in the galactic disk. The yellow shades represent the warm phase and the darker, red shades represent the hotter, less dense hot phase. The mean field lines are generally aligned in the azimuthal (y) direction and mostly span the box along the y-axis. We can see in panels (a) and (b) that, in the warm phase, the displacements of the field lines in the x and z directions are much smaller those along the y direction. On the other hand, distortions of the field lines in the hot gas are rather strong. There is a hot gas bubble clearly visible in panel (c) in the range $0.7 < z < 1$ kpc, where the mean field lines are wrapped around it. This suggests that the hot gas, which typically exhibits transonic turbulence, has sufficient kinetic energy to distort the magnetic field lines as it expands and travels out of the box. Further, we note a column of hot gas spanning the z axis in the box, in the corner ($y = -0.5$ kpc, $x = 0.5$ kpc). We note that the field lines are distorted to avoid entering the hot column. Since SNe typically occur within 0.1 kpc of the galactic midplane (Gent, 2012), turbulent kinetic energy is injected into the ISM close to the midplane. If multiple SNe occur close to each other, they can join to form a superbubble producing a chimney-like structure (Gent, 2012)

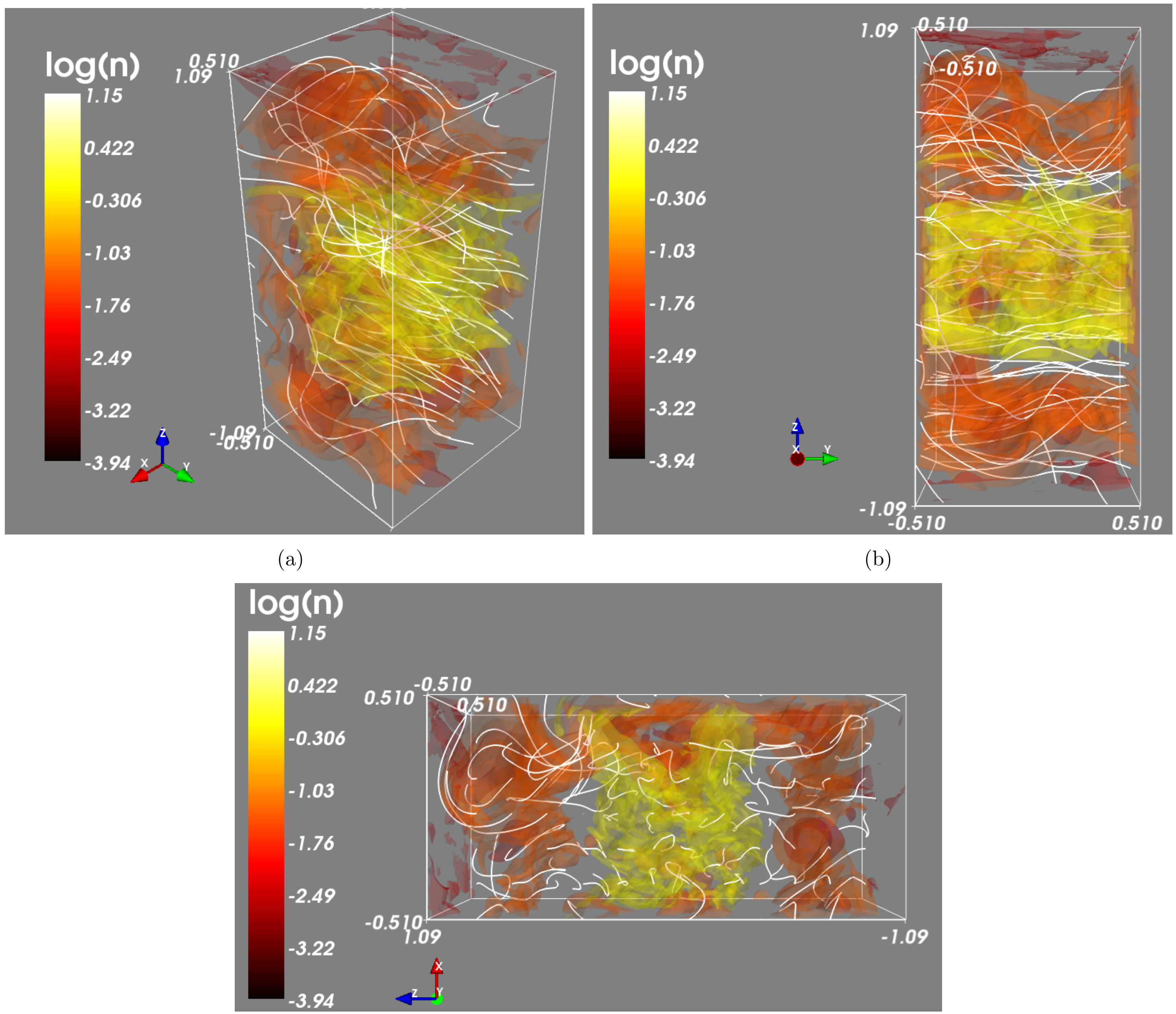

(a)

(b)

(c)

Figure 3.1: 3D rendering of mean magnetic field lines (white lines) in the simulated ISM gas 1.4 Gyr after the start of the simulation, with gas density colour coded. Panel **(a)** gives an isometric view, whilst panels **(b)** and **(c)** give a view along the x and y axes, respectively.

similar to the column observed in Fig. 3.1.

3.2 Statistical analysis of the multi-phase structure

As discussed in Section 3.1, the mean field is generally aligned with the azimuthal (y) direction. We use an idea from the field of stereology, which states that, for a statistically homogeneous random field, samples taken from the entire volume and along arbitrary lines through it are statistically equivalent (Baddeley and Jensen, 2004).

Apart form the overall stratification, there are no reasons to expect that the gas, in the relatively small computational that we have, deviates from statistical homogeneity. Thus, samples along magnetic lines should lead to average characteristics of the gas distribution consistent with those derived from volume and time averaging.

Since we sample specific entropy along the magnetic field lines, we can clarify the sensitivity of the magnetic field to the multi-phase structure. An important feature of the mean magnetic field, strongly suggested by theory but never verified observationally or in numerical simulations, is that it is generated by the turbulent dynamo action in the warm gas (Shukurov, 2007). The cold phase occupies too small a volume to be a host of the global dynamo action. The hot phase is unsteady, with the hot gas leaving the galactic disc for the halo at a time scale shorter than the dynamo time scale.

However, it is difficult to verify this suggestion. Magnetic energy is not suitable for this since most of the gas mass is in the cold phase, which biases the energy distribution very strongly. Enhanced local velocity shear produces a similar bias in the hot phase.

We suggest a new approach to probing the relation of the magnetic field to the multi-phase structure, based on the relative fraction of the magnetic field line length in each phase. The question we are able to address is; do magnetic field lines of the mean field prefer any of the phases? If so, which phase does it prefer? Is there any difference between the mean and random magnetic field lines in this respect?

To answer these questions, we compute the PDFs of specific entropy along magnetic field lines and along straight lines. We expect that any bias of the magnetic field, with respect to the multi-phase structure, will be visible in the PDFs. Moreover, for the straight line sampling the probability of each phase must be equal to its fractional volume, which is easy to calculate by volume averaging. This provides an essential control of the method.

3.2.1 The phase that hosts the mean field

The sampled specific entropy data from the the field lines and straight lines, from the snapshot at $t = 1.4$ Gyr, are used to derive PDFs of specific entropy, s, for straight lines and mean field lines shown in Fig, 3.2. The fractional volume

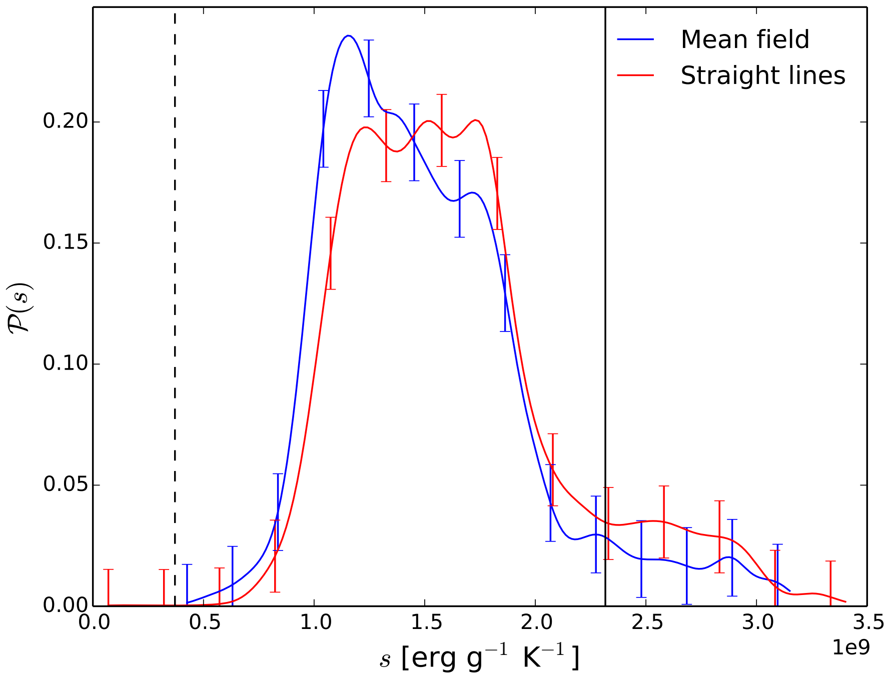

(a)

Figure 3.2: The PDF of specific entropy, s, sampled along mean field lines (blue solid) and straight lines (red solid). The vertical lines represent the cold-warm and warm-hot phase boundaries. The data is taken from the snapshot at $t = 1.4$ Gyr.

of the cold phase is less than 0.01 (Gent, 2012), so it is hardly visible in this representation.

The warm-hot phase boundary is represented by a solid black vertical line in Fig. 3.2. The fractional volume of the warm phase, $f_{\mathrm{v,warm}}$ is generally between 0.88 and 0.96 in the midplane and the fractional volume of the hot phase, $f_{\mathrm{v,hot}}$, is generally between 0.04 and 0.12, once the numerical model has reached the statistically steady phase. Hence, we expect the statistical properties of the warm phase to dominate the PDFs.

At $t = 1.4$ Gyr, the PDF of s along the mean field lines, hereafter referred to as $\mathcal{P}_B(s)$, has higher probability density in the cooler, denser regions (3.7 erg g^{-1} K^{-1} $<$

$s < 15$ erg g^{-1} K^{-1}) of the warm phase. The PDF of s along straight lines, hereafter referred to as $\mathcal{P}_-(s)$, is higher than $\mathcal{P}_B(s)$ in the hotter, more turbulent ($s > 1.5 \cdot 10^9$ erg g^{-1} K^{-1}) regions of the multi-phase.

Moreover, we note that $\mathcal{P}_-(s)$ extends to higher s in the hot phase; whilst the maximum entropy observed along mean field lines is approximately $s = 3.1 \cdot 10^9$ erg g^{-1} K^{-1} the maximum entropy observed along straight lines is $s = 3.5 \cdot 10^9$ erg g^{-1} K^{-1}. In a bubble or other cluster of hot gas, we typically expect the higher entropies to be observed inside the cluster, whereas lower entropies would be observed close to the boundary of the cluster due to optically thin cooling of the gas bubble at the boundary of the bubble. The mean magnetic field lines reside in the cooler regions of the warm phase. The distortions of the mean field lines featured in the hot phase, especially around SN remnants, renders the hot phase an unsteady environment for the global dynamo.

We previously observed that the mean field lines are wrapped around the clusters of hot gas and do not tend to pass through the clusters, due to the distorting effect of the hot gas cluster on the mean field. On the other hand, straight lines in the azimuthal direction are not sensitive to the multi-phase structure and can pass through the hottest parts of clusters of hot gas. Consequently, the lower maximum s observed along mean field lines suggests that the mean field lines do not pass through the hottest regions of the ISM gas and thus the higher s values are not observed along the mean field lines. When the mean magnetic field is wrapped around the hot gas moving out of the box, it temporarily resides in a region of higher entropy; this behaviour amounts to forced advection of the mean field with the hot gas. Rather than passing through the hot gas, the mean field lines tend to change shape quite drastically. This interaction between the hot phase and the mean magnetic field lines are observed in all snapshots in the statistically-steady state of the model. It has been observed in 3D renderings of the mean field lines across all other snapshots (omitted in this report). Figure 3.3 shows $\mathcal{P}_B(s)$ and $\mathcal{P}_-(s)$ constructed in the $|z| < 0.75$ kpc region (panel (a)), where the warm phase is dominant, and in the $|z| > 0.75$ kpc region (panel (b)), where increased fractional volume of the hot phase causes distortions of the mean magnetic field lines.

The PDFs in panel (a) have similar shapes, with $\mathcal{P}_B(s)$ favouring lower entropies, as shown previously in Fig. 3.2. Whilst the modes of $\mathcal{P}_B(s)$ and $\mathcal{P}_-(s)$ are similar in panel (b), the differences of the shapes of the PDFs are more difficult to interpret.

The PDFs are more localised in this figure; they favour lower entropies in panel (a) and higher entropies in panel (b). $\mathcal{P}_B(s)$ continue to have higher probability density than $\mathcal{P}_-(s)$ at lower entropies in both panels.

The fractional volume of the hot phase is $f_{\mathrm{v,hot}} = 0.12$ at $t = 1.4$ Gyr. However, in the remaining ten snapshots taken at $t > 1.4$ Gyr, $f_{\mathrm{v,hot}} = 0.05$.

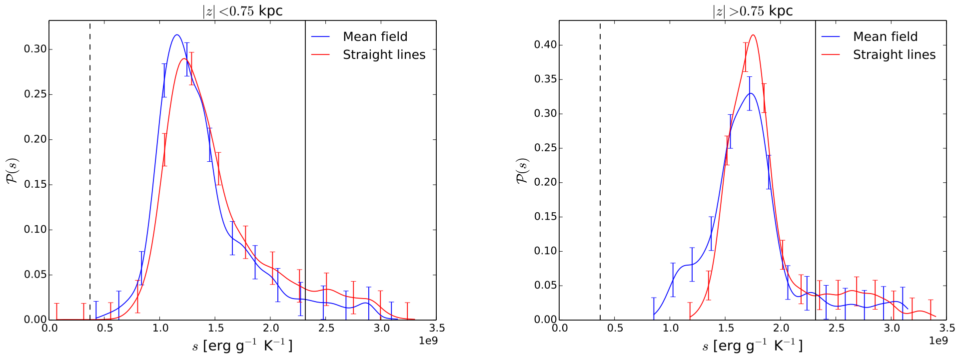

(a) (b)

Figure 3.3: $\mathcal{P}_B(s)$ and $\mathcal{P}_-(s)$ calculated in **(a)** $|z| < 0.75$ kpc and **(b)** $|z| > 0.75$ kpc at $t = 1.4$ Gyr.

	Whole box		$|z| < 0.75$ kpc		$|z| > 0.75$ kpc	
Phase	$\mathcal{P}_B(s)$	$\mathcal{P}_-(s)$	$\mathcal{P}_B(s)$	$\mathcal{P}_-(s)$	$\mathcal{P}_B(s)$	$\mathcal{P}_-(s)$
Cold	$\ll 0.01$	$\ll 0.01$	$\ll 0.01$	$\ll 0.01$	$\ll 0.01$	$\ll 0.01$
Warm	0.93	0.88	0.95	0.91	0.91	0.86
Hot	0.07	0.12	0.05	0.09	0.09	0.14

Table 3.1: Probabilities of mean field lines and straight lines being found in each phase, calculated in different ranges of z.

The characteristics of $\mathcal{P}_B(s)$ seen previously are retained in Fig. 3.4(a), where data from all twelve snapshots have been time averaged, despite the increase of $f_{\mathrm{v,warm}}$. $\mathcal{P}_B(s)$ and $\mathcal{P}_-(s)$ are very similar in $|z| < 0.75$ kpc (Fig. 3.4(b)) but the differences between them, seen in $|z| > 0.75$ kpc, are retained after time averaging (Fig. 3.4(c)). The probabilities of the mean field lines and straight lines being found in each phase, for the snapshot at $t = 1.4$ Gyr, are reported in Table 3.1. The mean field lines have a higher probability of passing through the warm phase than straight lines, regardless of the z range in consideration. This result is also obtained for the probabilities calculated after time averaging. In addition, the sampling along straight lines consistently calculates probabilities matching the fractional volumes of the phases, as expected.

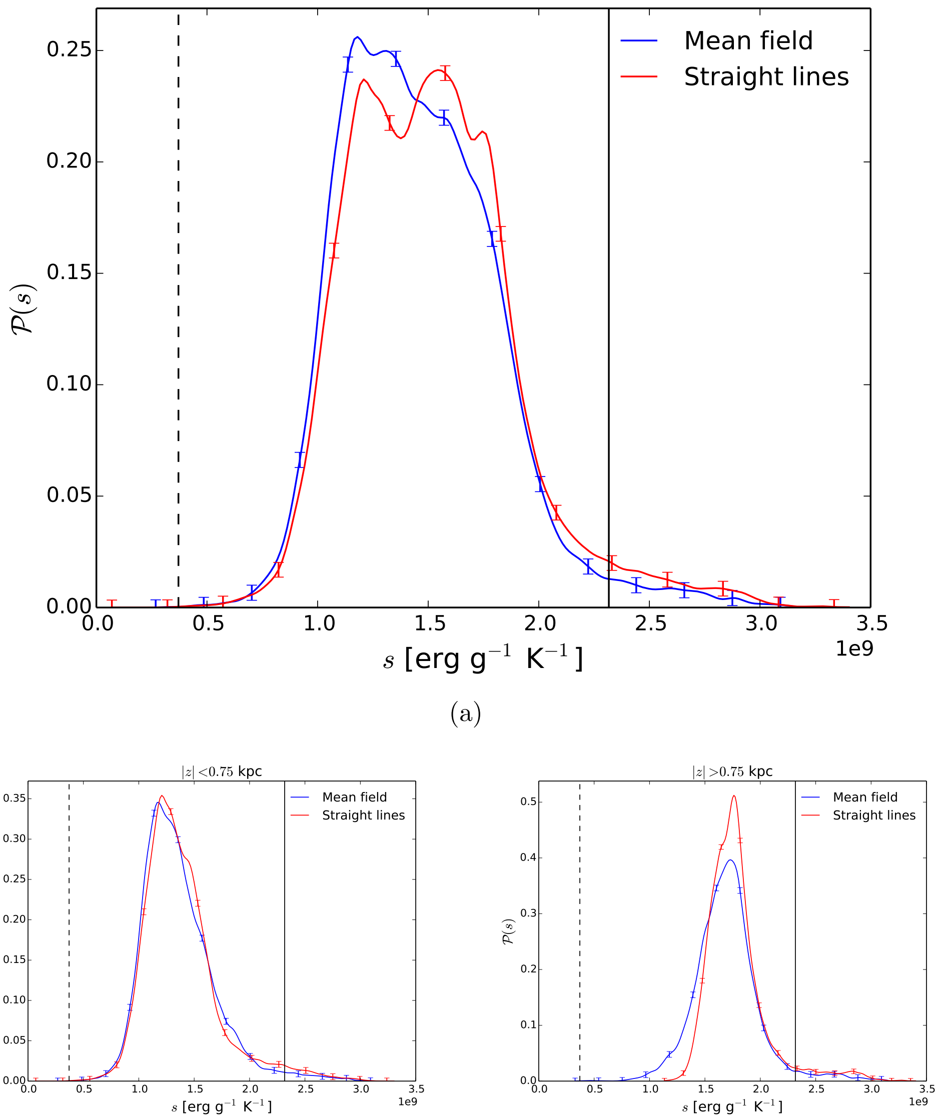

(a)

(b)

(c)

Figure 3.4: $\mathcal{P}_B(s)$ and $\mathcal{P}_{-}(s)$ calculated in **(a)** $|z| < 1$ kpc **(b)** $|z| < 0.75$ kpc **(c)** $|z| > 0.75$ kpc at $t = 1.4$ Gyr.

3.2.2 The random magnetic field

The typical length scale of SN remnants and other hot gas structures propagating through the box is similar to the typical length scale of mean magnetic field lines. The random magnetic field represents the fluctuations in the magnetic field,

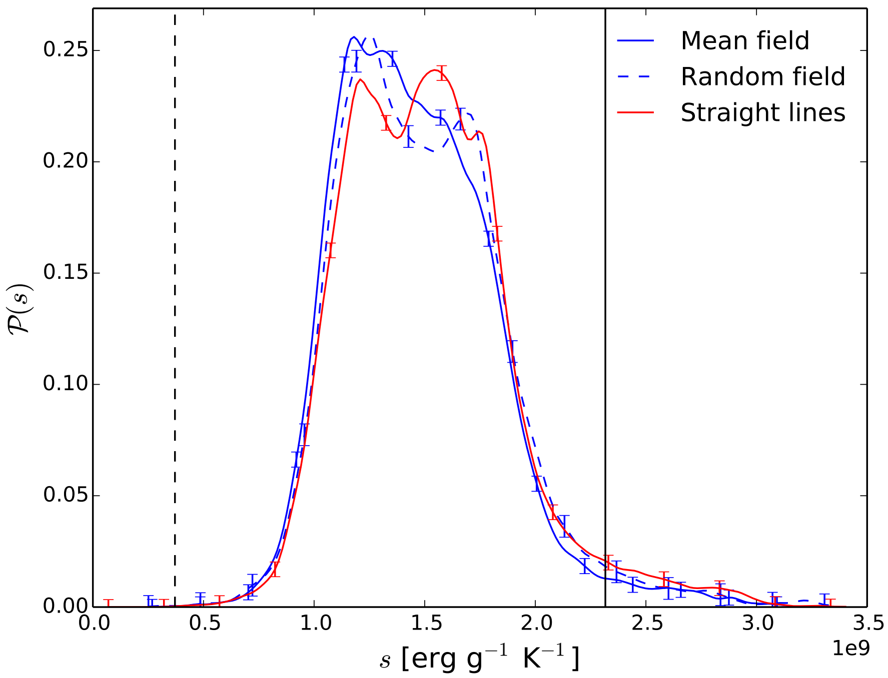

Figure 3.5: PDFs of entropy sampled along mean magnetic field lines (blue solid), random magnetic field lines (blue dashed) and straight lines (red solid). All twelve snapshots of the steady-phase of the model are used to calculate these PDFs.

which occur over smaller length scales. Therefore, we do not expect the geometry of the random magnetic field lines to be particularly sensitive to the multi-phase structure. However, the typical strengths of the mean and random magnetic fields should be sensitive to the multi-phase structure and distance from the galactic mid-plane. We construct a PDF of entropy sampled along random magnetic field lines, denoted by $\mathcal{P}_b(s)$ which is presented in Fig. 3.5 alongside $\mathcal{P}_B(s)$ and $\mathcal{P}_-(s)$ sampled across the twelve snapshots available. The PDF of entropy sampled along random field lines, hereafter referred to as $\mathcal{P}_b(s)$, is bimodal, with both modes in the warm phase. Its first mode is at $s = 1.2 \cdot 10^9$ erg g^{-1} K^{-1}, a slightly higher entropy than the mode of $\mathcal{P}_B(s)$. The second mode is at $s = 1.7 \cdot 10^9$ erg g^{-1} K^{-1}, in the hotter, less dense region of the warm phase. $\mathcal{P}_b(s)$ has lower probability density than $\mathcal{P}_B(s)$ for $s < 1.2 \cdot 10^9$ erg g^{-1} K^{-1}. However, the difference between the two PDFs is small at these entropies. At higher entropies, $\mathcal{P}_b(s)$ has greater probability density and extends to higher entropies. This suggests that the random field is not as sensitive to the multi-phase structure as the mean field.

3.3 Supernova remnants

An SN remnant is identified in the $0.7 < z < 0.9$ kpc region of the box at $t = 1.4$ Gyr. A horizontal slice of the box is taken at $z = 0.798$ kpc, which captures a slice through the SN remnant. We then look at colourmap images of various physical variables with integral lines of (B_x, B_y) overlaid.

3.3.1 Thermal pressure in SN remnants

Figure 3.6 shows the colour map image of logarithmic thermal pressure, $\log(p)$, on the horizontal slice taken at $z = 0.798$ kpc at $t = 1.4$ Gyr. integral lines of the horizontal mean magnetic field are overlaid with the colour of the integral lines representing mean magnetic field energy. Thermal pressure is used to identify

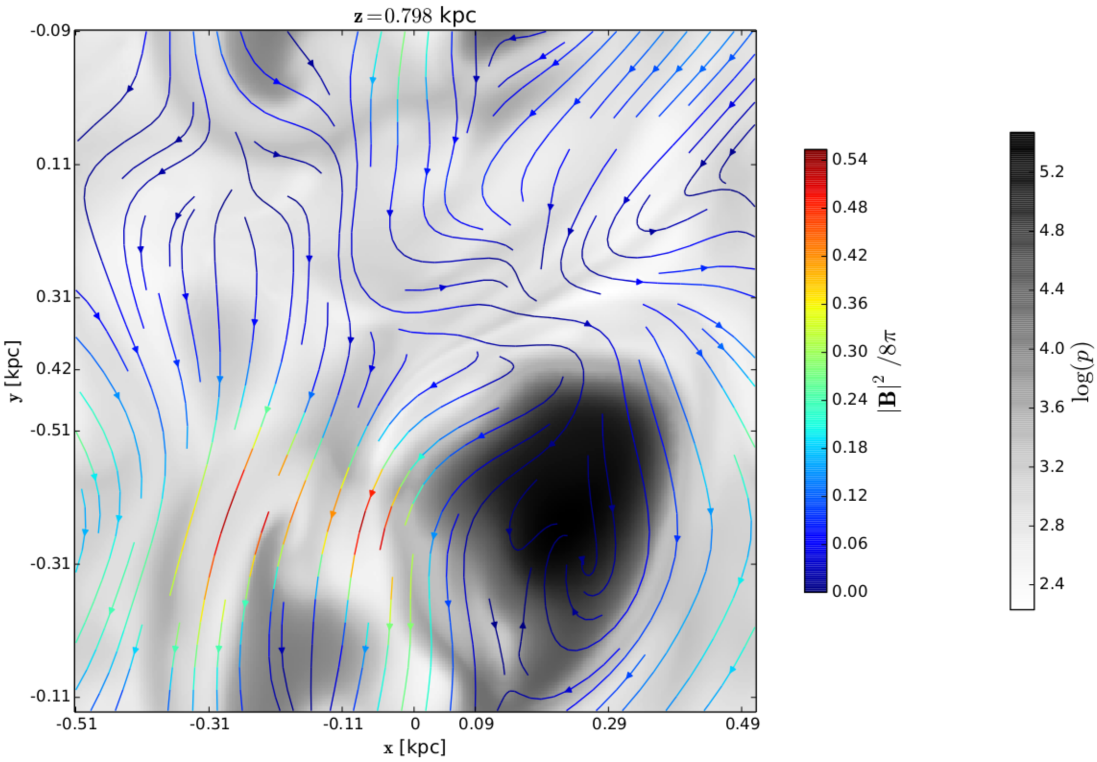

Figure 3.6: Thermal pressure (colour coded) with integral lines the horizontal magnetic field at $z = 0.798$ kpc.

the SN remnant, with extremely high thermal pressures observed inside the SN remnant and a high pressure gradient at the boundaries of the SN remnant. We observe this structure in the bottom right corner of the image. The thermal pressures observed at this slice are typical of the warm and hot phases and we observe values over three orders of magnitude. The highest pressures are observed at the center of the SN remnant. We note that, whilst the pressure is high along the boundary, it is noticeably lower than the pressure at the center. In general, the mean magnetic field is very weak across the slice; it is very weak inside the SN remnant. In addition, we observe that the magnetic field lines generally span the slice in the azimuthal (y) direction, forming long structures.

Moreover, the left half of the box is largely unaffected by the SN remnant. Consequently, the mean field integral lines are straighter and less distorted. Conversely, the mean field lines near the SN remnant are wrapped around it. In the right half of the image, we notice that the mean field integral lines still span the slice in the y-axis. Yet, they are more perturbed than the lines in the left half, due to the distortions caused by the SN remnant. The correlation of points along the magnetic field implies that the distortions caused in a particular region of the magnetic field can affect the magnetic field structures at large distance, presumably due to magnetic tension.

3.3.2 Gas velocity magnitude in SN remnants

Figure 3.7 shows the gas velocity, $|\boldsymbol{u}|^2$, in the horizontal slice at $z = 0.798$ kpc, $t = 1.4$ Gyr. Integral lines of the mean horizontal magnetic field are overlaid with the colour of the integral lines representing specific entropy. Both the highest velocities and entropies are observed near the center of the SN remnant. The highest specific entropy, $s \approx 3.5 \cdot 10^9$ erg g^{-1} K^{-1}, corresponds to the maximum specific entropy observed along the straight line in Fig. 3.2. The maximum entropy close to the boundary of the SN remnant, $s \approx 3.1 \cdot 10^9$ erg g^{-1} K^{-1}, corresponds to the maximum entropy that $\mathcal{P}_B(s)$ extends to in the hot phase in Fig. 3.2.

The SN remnant is characterised by high kinetic energy, high entropy and low density. The high pressure gradients across the boundary of the SN remnant and its buoyancy cause the rapid outflows of hot gas, which explains the complete dominance of the hot phase at $|z| > 2.5$ kpc region.

3.4 Correlation lengths

To test further the reliability of statistical results obtained from our analysis along magnetic field lines, we calculate correlation lengths of the mean and random magnetic field lines in terms of maximum distance from the seed point and maximum displacement from the seed point in the x, y and z directions, denoted by $\mathcal{C}$, $\mathcal{C}_x$,

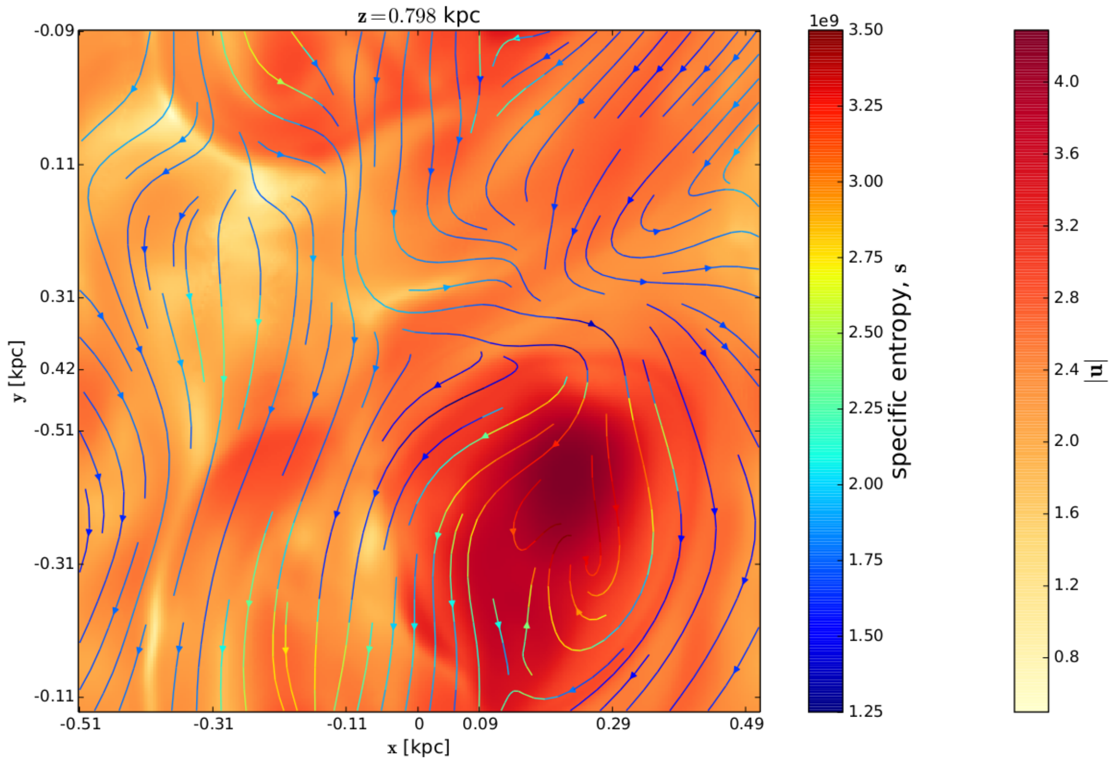

Figure 3.7: Gas velocity magnitude with integral lines of (B_x, B_y) at $z = 0.798$ kpc, $t = 1.4$ Gyr.

$\mathcal{C}_y$ and $\mathcal{C}_z$, respectively. These values are summarised in Table 3.2 below. We note that the maximum distances in the x, y and z directions do not necessarily occur at the same point as the maximum distance from the seed point. Thus, we do not expect $\mathcal{C} = \left(\mathcal{C}_x^2 + \mathcal{C}_y^2 + \mathcal{C}_z^2\right)^{1/2}$ to hold, unless all maxima occur at the same point along the field line. We observe that the correlation length for the mean field lines is a factor of five larger than for the random field lines. The ratio $\mathcal{C}_B/\mathcal{C}_b$ can be used to analyse the sensitivity of the field line integration to the averaging kernel scale and to optimise the separation of the mean and random magnetic field.

$\mathcal{C}_y$ is significantly larger for the mean field, even with the effect of differential rotation taken into account. This reinforces the predominantly azimuthal nature of the mean field. $\mathcal{C}_x$ and $\mathcal{C}_z$ are also larger for the mean field, albeit to a lesser extent than $\mathcal{C}_y$. This can be explained by the distortions caused in the mean field. Otherwise, we do not have any reasons to expect different correlation lengths in the x and z axes between the mean and random fields. However, this preliminary

	Correlations [kpc]	
	Mean field	Random field
$\mathcal{C}$	0.735	0.141
$\mathcal{C}_x$	0.045	0.034
$\mathcal{C}_y$	0.382	0.046
$\mathcal{C}_z$	0.085	0.050

Table 3.2: Correlation lengths for the mean and random magnetic field lines from an ensemble average of twelve snapshots of the ISM simulation (Gent, 2012).

result will be investigated further in the future.

We note that the correlation lengths of the random field along the axes are very similar, which suggests that the random magnetic field is isotropic (or at least approximately isotropic). This reinforces the argument that the random magnetic field is not as sensitive to the multi-phase structure as the mean magnetic field, since it does not appear to be affected by the turbulent random flows, differential rotation or strong inhomogeneity of the gas. The PDF of correlation lengths for

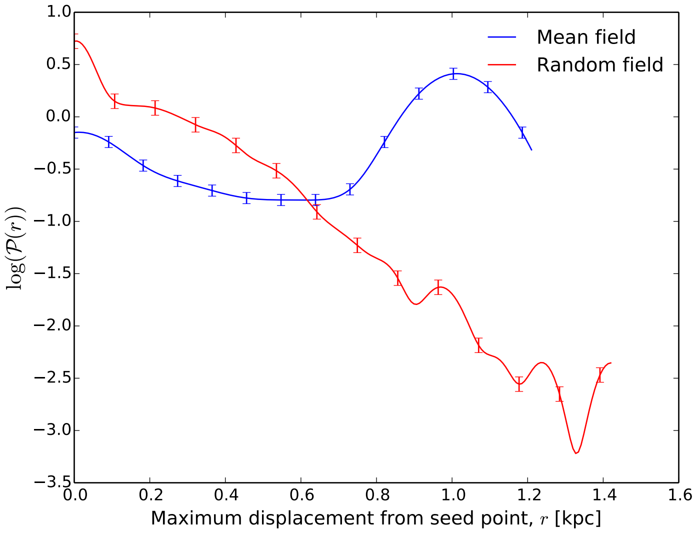

Figure 3.8: PDFs of correlation lengths for mean (blue) and random (red) field lines.

mean and random field lines are given in Fig. 3.8. The characteristic, modal correlation length for mean field lines is 1 kpc. The PDF is localised about this value, with the probability density low outside 0.8 kpc $< \mathcal{R} <$ 1.2 kpc.

For the random field. most of the probability density lies in 0 kpc $< \mathcal{R} <$ 0.6.

Longer correlations are observed with very low probability. These longer random field lines are likely to be artefacts arising from the numerical integration scheme. However, they occur very rarely and subsequently do not affect the statistical analysis.

The methods developed in this report show the mean field to be predominantly azimuthal. The only deviation from this is due to the distortion caused by hot gas. However, the geometry of the random field lines is still not fully explored. We require methods which are sensitive to the topology of random field to explore this.

Chapter 4

Conclusion

Our results provide the first clarification of the sensitivity of magnetic fields to the multi-phase structure of the interstellar gas in simulations of the supernova-driven interstellar medium.

We argue that the energy density of the magnetic field is a poor diagnostic in the multi-phase gas because most of its mass is in the cold phase but most of the velocity shear is in the hot gas; the gas pressure is nearly the same in all the phases.

To reveal the effects of the multi-phase gas structure on the mean and random magnetic fields, we develop a new approach of statistical analysis of the gas properties along the integral lines of the two parts of the magnetic field. In particular, we analyse the probability density of the specific entropy along magnetic lines. Specific entropy is ued to separate the phases, with lower values in the cold gas, intermediate in the warm phase and the highest entropy in the hot regions. We also calculate the probability density alomg randomly positioned straight lines through the domain to find out the nature of any biases in the behaviour of the magnetic field lines.

4.1 Planned work

We plan to analyse the effect of adding cosmic rays to the model using the methods developed in this report. The results presented in this report are currently in preparation for publication in the Monthly Notices of the Royal Astronomical Society.

Bibliography

Computational Fluid Dynamics (CFD) Online, 2007. URL http://www.cfd-online.com/Wiki/Introduction_to_turbulence/Statistical_analysis/Probability#Histogram_and_probability_density_function.

Baddeley, A. and Jensen, E. *Stereology for Statisticians.* Chapman & Hall/CRC Monographs on Statistics & Applied Probability. Taylor & Francis, 2004. ISBN 9780203496817. URL http://books.google.co.uk/books?id=il0fXb_GSowC.

Bourke, P. Trilinear Interpolation, 1997. URL http://paulbourke.net/miscellaneous/interpolation/.

Brandenburg, A., Dobler, W., Lyra, W., and Haugen, N. E. L. Pencil Code, 2001.

de Avillez, M. A. and Breitschwerdt, D. Volume filling factors of the ISM phases in star forming galaxies. i. the role of the disk-halo interaction. *A&A*, 425:899–911, Oct. 2004.

de Avillez, M. A. and Breitschwerdt, D. Global dynamical evolution of the ism in star forming galaxies. i. high resolution 3d simulations: Effect of the magnetic field. *A&A*, 436:585–600, June 2005.

Eckart, A. and Englmaier, P. Galaxy structure. *Encyclopedia of Astronomy and Astrophysics*, 2002. URL http://eaa.crcpress.com/default.asp.

Fletcher, A., Beck, R., Shukurov, A., Berkhuijsen, E. M., and Horellou, C. Magnetic fields and spiral arms in the galaxy m51. *MNRAS*, 412(4):2396–2416, 2011. ISSN 1365-2966. URL http://dx.doi.org/10.1111/j.1365-2966.2010.18065.x.

Gent, F. A. *Supernova Driven Turbulence in the Interstellar Medium.* PhD thesis, Newcastle University School of Mathematics and Statistics, November 2012. URL http://hdl.handle.net/10443/1755.

Gent, F. A., Shukurov, A., Sarson, G. R., Fletcher, A., and Mantere, M. J. The supernova-regulated ISM - I. The multiphase structure. *MNRAS*, 432:1396–1423, June 2013a. doi: 10.1093/mnras/stt560.

Gent, F. A., Shukurov, A., Sarson, G. R., Fletcher, A., and Mantere, M. J. The supernova-regulated ISM - II. The mean magnetic field. *MNRAS*, 430:L40–L44, Mar. 2013b. doi: 10.1093/mnrasl/sls042.

Gutierrez-Osuna, R. Texas A&M University CSCE 666: Pattern Analysis Lecture Notes, 2013. URL `http://research.cs.tamu.edu/prism/lectures/pr/pr_l7.pdf`.

Hill, A. S., Joung, M. R., Mac Low, M.-M., Benjamin, R. A., Haffner, L. M., Klingenberg, C., and Waagan, K. Vertical Structure of a Supernova-driven Turbulent, Magnetized Interstellar Medium. *ApJ*, 750:104, May 2012.

Kern, R. SciPy Reference Guide: Gaussian kernel density estimation, 2005. URL `http://docs.scipy.org/doc/scipy/reference/generated/scipy.stats.gaussian_kde.html`.

Korpi, M. J., Brandenburg, A., Shukurov, A., Tuominen, I., and Nordlund, Å. A supernova-regulated interstellar medium: simulations of the turbulent multiphase medium. *ApJ*, 514:L99–L102, April 1999.

Kulsrud, R. M. Propagation of cosmic rays through a plasma. In A. Reiz & T. Andersen, editor, *Astronomical Papers Dedicated to Bengt Stromgren*, pages 317–326, 1978.

Parker, E. *Conversations on Electric and Magnetic Fields in the Cosmos*. Princeton Series in Astrophysics. Princeton University Press, 2013. ISBN 9781400847433. URL `https://books.google.co.uk/books?id=jbHtAQAAQBAJ`.

Sarson, G. R. MAS8122: Introduction to Numerical and Computational Modelling. "$https://blackboard.ncl.ac.uk/bbcswebdav/pid{-}1993819{-}dt{-}content{-}rid - 6237227\_1/courses/O1415 - MAS3122/application2.pdf$", 2014.

Shukurov, A. In Dormy, E. and Soward, A. M., editors, *Mathematical Aspects of Natural Dynamos*, pages 313–359. Chapman & Hall/CRC, 2007.

Tabatabaei, F. S., Krause, M., Fletcher, A., and Beck, R. High-resolution radio continuum survey of m 33. *A&A*, 490(3):1005–1017, 2008. doi: 10.1051/0004-6361:200810590. URL `http://dx.doi.org/10.1051/0004-6361:200810590`.

Tennekes, H. and Lumley, J. L. *First Course in Turbulence.* Cambridge: MIT Press, 1972.

Verveer, P. J. SciPy Reference Guide: Multi-dimensional image processing - "gaussian_filter1d" and "gaussian_filter", 2003. URL `http://docs.scipy.org/doc/scipy/reference/ndimage.html`.